minerals

MDPI

Article

Improved Understanding of the Sulfidization Mechanism in Amine Flotation of Smithsonite: An XPS, AFM and UV–Vis DRS Study

Ruizeng Liu [1], Bin Pei [1], Zhicheng Liu [2], Yunwei Wang [1], Jialei Li [1,*] and Dianwen Liu [1,*]

[1] Faculty of Land Resources Engineering, Kunming University of Science and Technology, Kunming 650093, China; liuruizeng@126.com (R.L.); Peibin14@126.com (B.P.); ljl219837@163.com (Y.W.)
[2] Chihong Technology & Engineering Co. Ltd., Qujing 655000, China; gu.dao@live.cn
* Correspondence: lijialei1993@foxmail.com (J.L.); dianwenliu@kmust.edu.cn (D.L.)

Received: 29 March 2020; Accepted: 17 April 2020; Published: 20 April 2020

Abstract: Sulfidization is required in the amine flotation of smithsonite; however, the sulfidization mechanism of smithsonite is still not fully understood. In this work, X-ray photoelectron spectroscopy (XPS), atomic force microscopy (AFM) and UV–vis diffuse reflectance spectroscopy (UV–vis DRS) were used to characterize sulfidized and unsulfidized smithsonite. The XPS and UV–vis DRS analyses showed that smithsonite sulfidization is a transformation of $ZnCO_3$ to ZnS on the smithsonite surfaces. However, this transformation is localized, resulting in the coexistence of $ZnCO_3$ and ZnS or in the formation of ZnS island structures on the sulfidized smithsonite surfaces. AFM height imaging showed that sulfidization can substantially change the surface morphology of smithsonite; in addition, AFM phase imaging demonstrated that sulfidization occurs locally on the smithsonite surfaces. Based on our findings, it can be concluded that smithsonite sulfidization is clearly a heterogeneous solid–liquid reaction in which the solid product attaches at the surfaces of unreacted smithsonite. Smithsonite sulfidization involves heterogeneous nucleation and growth of ZnS nuclei. Moreover, the ZnS might nucleate and grow preferentially in the regions with high reactivity, which might account for the formation of ZnS island structures. In addition, sphalerite-structured ZnS is more likely to be the sulfidization product of smithsonite under flotation-relevantconditions, as also demonstrated by the results of our UV–vis DRS analyses. The results of this study can provide deeper insights into the sulfidization mechanism of smithsonite.

Keywords: smithsonite; sulfidization; amine flotation; AFM; UV–vis DRS

1. Introduction

With the exhaustion of zinc sulfide resources, nonsulfide deposits are increasing in economic importance. Smithsonite is a typical nonsulfide zinc mineral, commonly referred to as "zinc oxide" mineral [1–4]. Many flotation methods employed for recovering zinc oxide minerals have been studied and applied, which involves pre-sulfidization or direct flotation using some collectors such as amines, xanthates, mercaptans, fatty acids and chelating agents [5]. Oxide minerals are well known to not floatas easily as their sulfide counterparts. In this regard, sulfidization flotation is widely used on an industrial scale for the treatment of zinc oxide ores. The sulfidization process converts the surface of oxide minerals into a sulfide surface. This process involves the dissolution, adsorption and chemical and/or electrochemical reactions [6]. After sulfidization, amines and xanthates can be used for the flotation of the zinc oxide minerals. However, further activation using metal ions such as Cu^{2+} and Pb^{2+} is required when xanthate is used as a collector [7–9]. In general, sulfidization amine flotation can achieve better performance, resulting in its wide use in industrial production [10,11].

As a vital stage in the flotation of zinc oxide minerals, sulfidization has been a topic of great interest. Using X-ray photoelectron spectroscopy (XPS), Garbassi and Marabini [12] demonstrated that ZnS forms on the surface of smithsonite at the expense of carbonate species expressed by Equation (1).

$$ZnCO_{3(s)} + S^{2-}{}_{(aq)} \rightarrow ZnS_{(s)} + CO_3{}^{2-}{}_{(aq)} \quad (1)$$

Other XPS studies conducted by Feng and Wen [2], Luo et al. [11] and Wu et al. [13] showed the formation of polysulfide species, in addition to ZnS. Zeta-potential measurements, another surface-sensitive technology, have shown that the addition of greater amounts of Na_2S makes the smithsonite zeta potential more negative and lowers its isoelectric point. The authors attributed this behavior to the formation of ZnS via chemical reactions of HS^- with the smithsonite surface ($pH_{IEP}(ZnS) \approx 2$; $6 \leq pH_{IEP}(ZnCO_3) \leq 8$) [5]. Time-of-flight secondary ion mass spectrometry (ToF-SIMS) analysis detected ZnS^-, ZnS^{2-}, S^- and $S_2{}^-$ on the surfaces of sulfidized smithsonite samples; and the corresponding depth profile analysis showed that the sulfidization product film thickness can reach more 10 nm [11], suggesting that smithsonite sulfidization is not confined to the smithsonite–aqueous solution interface, but continues within the bulk of particles. Density functional theory calculations have also been carried out to study the sulfidization flotation of smithsonite [14–16].

Numerous studies have attempted to elucidate the sulfidization mechanism of smithsonite [2,11,13–16]. However, most of them have only focused on the adsorption of sulfide or hydrosulfide ions on the smithsonite surface and failed to discuss the entire sulfidization process; little research has analyzed the crystal phase of the sulfidization product; in addition, a model of the sulfidized smithsonite particle has not been proposed yet. That is, the sulfidization mechanism is still unclear. In the present work, XPS, atomic force microscopy (AFM) and UV–vis diffuse reflectance spectroscopy (UV–vis DRS) were used to characterize sulfidized and unsulfidized smithsonite. The aim of the present work was to further elucidate the sulfidization mechanism in the amine flotation of smithsonite. The results can also provide deeper insights into the sulfidization mechanism in the smithsonite flotation with metal ions as activator and xanthate as collector.

2. Materials and Methods

2.1. Materials

The smithsonite sample was purchased from Yunbaozhai, a jewels and mineral specimens store in Kunming, China. The sample was handpicked, crushed with a hammer, ground in an agate mortar and screened to obtain the −75 +38 μm size fractions for flotation, XPS and UV–vis DRS tests. Chemical analysis showed that the sample contained 50.35 wt% Zn, indicating a purity of 96.5% $ZnCO_3$. The X-ray diffraction (XRD) pattern (Figure 1a) of the powder sample could match the standard pattern for smithsonite $ZnCO_3$ (JCPDS No. 08-0449), and no impurity peaks could be observed. Bulk specimens (approximately $1 \times 1 \times 0.2$ cm^3 in length, width and depth) for AFM observations were prepared using the method described in previous work [10].

Dodecylamine hydrochloride (DDA, $C_{12}H_{27}N{\cdot}HCl$) was used as a collector and frother; sodium sulfide ($Na_2S{\cdot}9H_2O$) was used as a sulfidizing agent; sodium hydroxide (NaOH) and hydrochloric acid (HCl) were used as pH regulators.

A pure ZnS sample was synthesized as a reference sample for use in the UV–vis DRS analysis. First, 100 mL of 0.1 mol/L $Na_2S{\cdot}9H_2O$ was mixed with 100 mL 0.1 mol/L $ZnSO_4$. After continuous stirring at 25 °C for 2 h, the formed precipitate was collected by filtration and then washed several times with deionized water. The final product was dried at 40 °C for 4 h. The XRD pattern of the synthesized sample matches with the data in JCPDS card no. 77–2100, showing a sphalerite ZnS phase.

Deionized water (18.3 MΩ cm) was used in all experiments. All of the aforementioned reagents were of analytical grade.

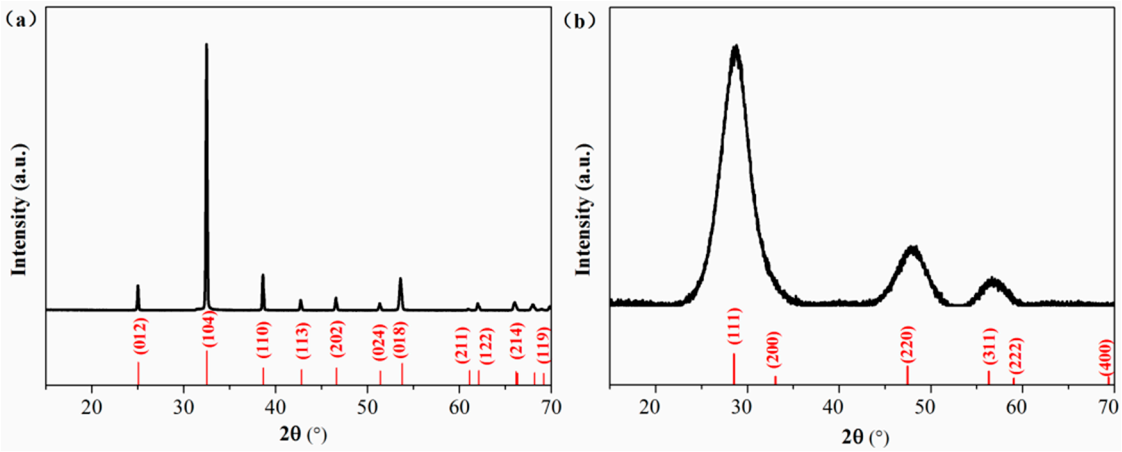

Figure 1. XRD patternsfor (**a**) the smithsonite sample and (**b**) synthetic sphalerite ZnS. Measured XRD patterns and JCPDS patterns were plotted in black and red, respectively.

2.2. Flotation Tests

Flotation tests were conducted in a 40 mL flotation cell (XFG flotation machine, Jilin Prospecting Machinery Factory, Changchun, China) at around 20 °C. In each flotation test, the mineral suspension was prepared by dispersing a 2.0 g mineral samples in deionized water in the cell. After being stirring for 1 min, Na_2S (if needed, stirring for 5 min), pH regulators (stirring for 2 min) and DDA (stirring for 3 min) were added separately to the pulp in sequence. After pH adjustment and before the addition of DDA, the pH values were measured by use of a pH meter and reported (PHBJ-260F, Rex Electric Chemical, Shanghai, China). After the 3 min of flotation, the floated and unfloated fractions were collected, filtered, dried and weighed to calculate the recovery. Each test was carried out in triplicate, and their mean value and standard deviation were calculated and plotted.

2.3. Characterization

The sulfidization treatment of smithsonite powder samples for XPS and UV–vis DRS measurements was same as that used in the flotation test. After treatment, the unsulfidized and sulfidized smithsonite particles were washed three times with deionized water and dried in a drying oven. Prior to measurements, the prepared sample were sealed in nitrogen to minimize oxidation. The XPS measurements were performed in a spectrometer (PHI5000 Versa Probe II, ULVAC-PHI, Inc., Kanagawa, Japan) equipped with an Al Kα X-ray source (1486.7 eV), and the C1s peak at 284.80 eV was used to calibrate the recorded spectra. The UV−vis DRS measurements of the samples were performed with a U-4100 UV–vis/near-infrared (NIR) spectrophotometer (Hitachi, Tokyo, Japan).

A slightly different sulfidization treatment was applied to bulk specimens for AFM observation. First, 2.0 g of smithsonite powders and a bulk specimen were soaked in a desired volume of deionized water. After agitation for 1 min, a Na_2S solution at the desired concentration was injected into the slurry. After sulfidization, the bulk specimen was washed three times with deionized water and then dried in a vacuum dryer. This sample preparation procedure was adopted to make the test conditions mimic the flotation conditions. AFM observations were performed with a Bruker Dimension Edge system (Bruker, Santa Barbara, CA, USA) operated in tapping mode. The height profile and phase shifts data were obtained using the NanoScope Analysis software (Version 1.40, Bruker, Santa Barbara, CA, USA).

3. Results and Discussion

3.1. Flotation Test

Figure 2 shows the flotation recovery of unsulfidized and sulfidized smithsonite as a function of the DDA concentration at pH 10.3. The flotation recovery of unsulfidized smithsonite gradually increased with increasing DDA concentration; however, the desired flotation performance could not

be attained. Compared with the flotation recovery of unsulfidized smithsonite, that of smithsonite treated with 5×10^{-4} mol/L Na_2S solution was substantially greater in the whole investigated DDA concentration range; in particular, a recovery of approximately 85% was achieved with 1.5×10^{-3} mol/L DDA as collector. Figure 3 shows a plot of the effect of Na_2S concentration on the smithsonite flotation with a DDA concentration of 1.5×10^{-3} mol/L at pH 10.3. As depicted in Figure 3, the recovery increased dramatically as the Na_2S concentration was increased to 2.5×10^{-3} mol/L. When the Na_2S concentration exceeded 2.5×10^{-3} mol/L, recoveries greater than 90% were achieved. These flotation results highlight that sulfidization is required in the amine flotation of smithsonite.

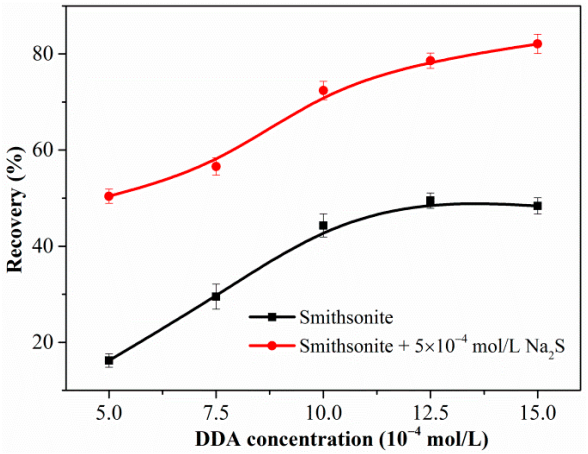

Figure 2. Flotation recovery of smithsonite as a function of DDA concentration in the absence or presence of Na_2S at pH 10.3.

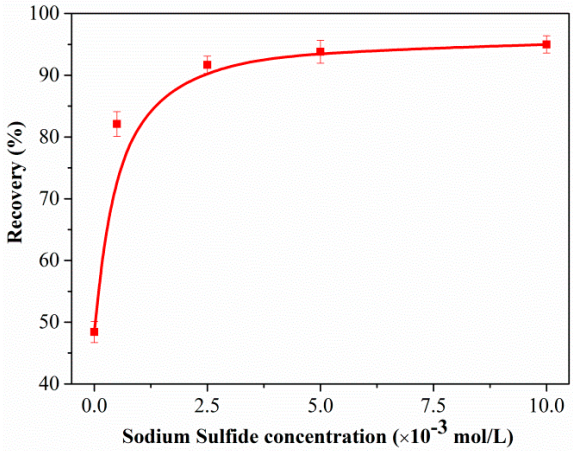

Figure 3. Flotation recovery of smithsonite as a function of Na_2S concentration C(DDA) = 1.5×10^{-3} mol/L, pH = 10.3.

3.2. XPS Measurement

Figure 4 plots the survey scan spectra of smithsonite treated with Na_2S solutions with different concentrations; peaks of C, O and Zn are observed. In the spectrum of the unsulfidized smithsonite, neither S2s or S2p peaks are observed (Figure 4a). However, after an aqueous Na_2S solution treatment, both S2s and S2p peaks appeared (Figure 4b–d), clearly showing that sulfidization had taken placed on the smithsonite surfaces [17].

For further information, we recorded detail-scan XPS spectra of sample surfaces, including their C1s, O1s, Zn2p3 and S2p spectra. As plotted in Figure 5a, the recorded C1s spectra were all fitted with two contributions. One was contributed by the adventitious carbon contamination, consisting of the peaks at 284.80 eV (C–C, C=C and C–H) and the peaks at ~286.30 eV (C−O single bond) [18–20]. Another, i.e., the peaks at ~290.0 eV, was attributed to carbonate in the smithsonite lattice [2,11].

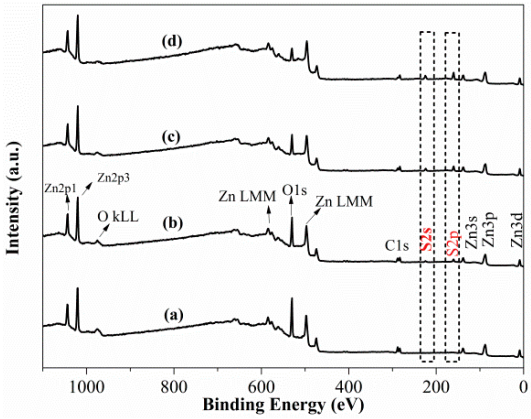

Figure 4. XPS survey scan spectra of smithsonite treated with (**a**) 0, (**b**) 0.5×10^{-3}, (**c**) 2.5×10^{-3} and (**d**) 10×10^{-3} mol/L $Na_2S{\cdot}9H_2O$.

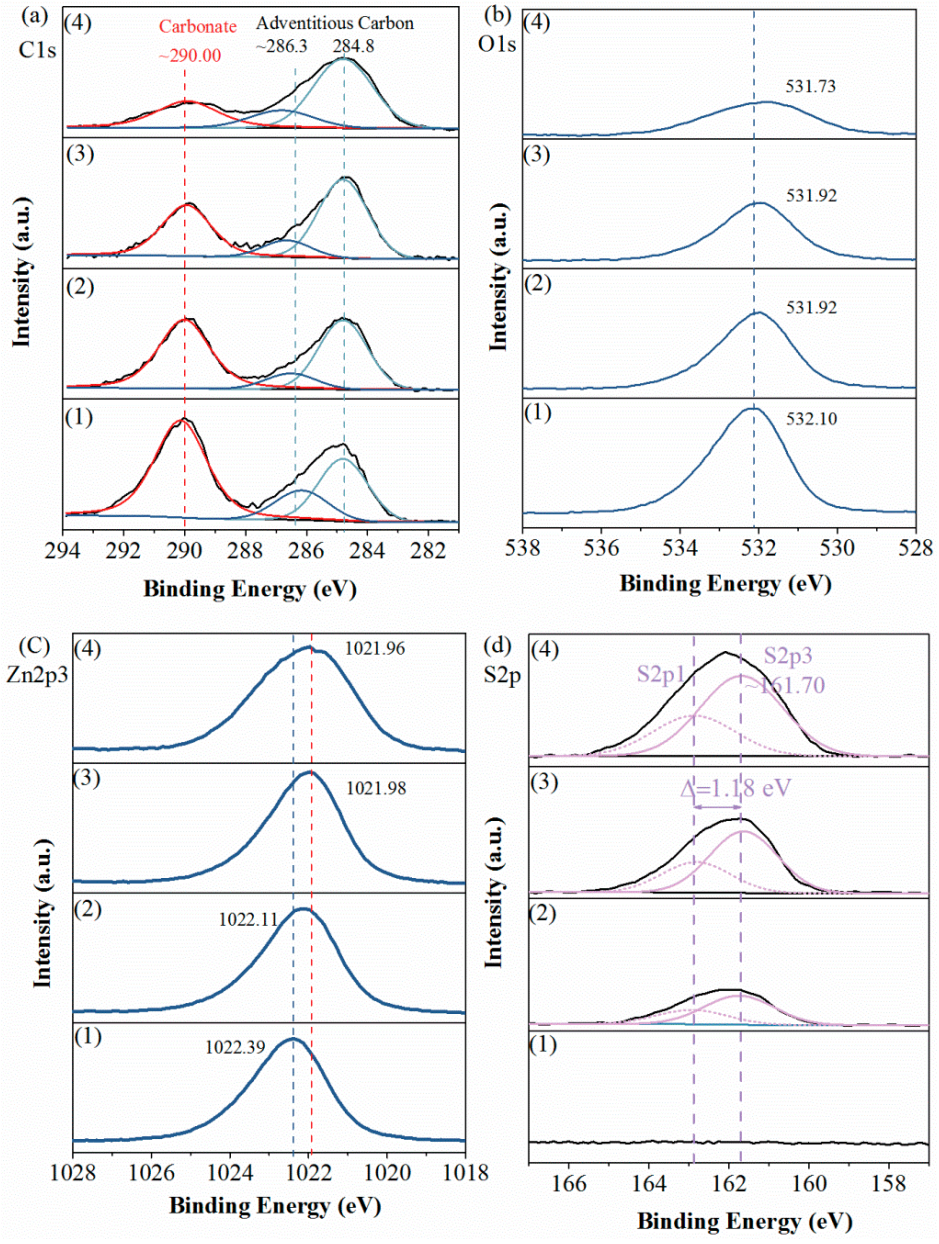

Figure 5. Detail-scans of (**a**) C1s, (**b**) O1s, (**c**) Zn2p3 and (**d**) S2p spectra of smithsonite treated with (1) 0, (2) 0.5×10^{-3}, (3) 2.5×10^{-3} and (4) 10×10^{-3} mol/L $Na_2S{\cdot}9H_2O$.

In the O1s spectra (Figure 5b), peaks showed at binding energies of 531.73–532.10 eV, which were mostly contributed by O in the carbonate of smithsonite. As the Na_2S concentration increased, the intensities of the C1s and O1s peaks that were contributed by the carbonate ions decreased substantially, indicating a significant decrease in carbonate concentration.

Figure 5c shows the Zn2p3 spectra of samples. In the spectrum of the unsulfidized smithsonite, a peak was observed at 1022.39 eV. As the Na_2S concentration was increased, the binding energy of Zn2p3 decreased from 1022.39 to 1021.96 eV, showing only a small shift in binding energy; furthermore, no obvious change was observed in the peak intensity. However, the peak broadened as the Na_2S concentration increased, hinting at the presence of more than one Zn species [21].

As shown in the S2p spectra (Figure 5d), as the Na_2S concentration was increased, the intensity of S2p peaks clearly increased, indicating that the S concentration increased. The recorded S2p peaks were fitted with a spin–orbit doublet comprising S2p3 and S2p1 (Δ = 1.18 eV), and the 2p3-to-2p1 peak-area ratio was fitted to the expected value of 2:1. The three fitted S2p3 peaks at ~161.70 eV were attributed to the sulfide in ZnS, which was consistent with the previous works (160.80 [22], 161.80 [23], 161.50 [24] and 161.65 [25] eV). However, we found no polysulfides species on the sample surfaces, which was inconsistent with previous works [2,11,13]. We inferred that the formation of polysulfides species was because of the slight oxidation of sulfidization product surfaces.

In general, larger chemical shifts could be observed for the peaks in the Zn LMM spectra than for those in the Zn2p spectra. Hence, Auger spectra (Zn LMM) were also recorded. As plotted in Figure 6a, the kinetic energy of the Zn LMM peak of the unsulfidized smithsonite was 987.21eV; however, the kinetic energy increased from 987.21 to 988.51 eV with increasing Na_2S concentration, revealing larger chemical shifts than those in the Zn2p3 spectra, as expected. In addition, Figure 6b shows the modified Auger parameter values reported in the present work and the literature [26]; these values were more sensitive to differences in the chemical environment. For the unsulfidized smithsonite, the Zn2p3 binding energy, Zn LMM kinetic energy and the modified Auger parameter were in good agreement with those reported in the literature for $ZnCO_3$ [26]. Interestingly, after sulfidization, the modified Auger parameter values in the present work were close to but did not reach the ZnS data region, indicating the co-existence of $ZnCO_3$ and ZnS on the sulfidized smithsonite surfaces.

To illustrate the smithsonite surface changes before and after sulfidization more intuitively, the atomic concentration and atomic ratio were calculated, as shown in Figure 6c,d, respectively. For the unsulfidized smithsonite, the concentrations of total C, CO_3^{2-}, O and Zn were 31.40%, 17.74%, 52.05% and 17.65%, respectively, and the CO_3^{2-}-to-Zn ratio and O-to-Zn ratio were 1.07 and 3.15, respectively, which were close to the expected values for $ZnCO_3$. After sulfidization, however, the chemical components at the smithsonite surfaces were significantly changed. The concentrations of total C, CO_3^{2-} and O decreased while the concentrations of Zn and S increased, with increasing concentration of Na_2S. After sulfidization, the increase in the Zn concentration on the sample surfaces was because the ZnS exceeded $ZnCO_3$ in zinc content. In addition, the O-to-Zn ratio and CO_3^{2-}-to-Zn ratio decreased while the S-to-Zn ratio increased, with increasing Na_2S concentration. However, the atomic ratio ($[CO_3^{2-}]$ + [S])/[Zn] was consistently close to 1.

In summary, these findings clearly show a transformation of $ZnCO_3$ to ZnS during smithsonite sulfidization; however, this transformation is localized, resulting in the coexistence of $ZnCO_3$ and ZnS on the sulfidized smithsonite surfaces.

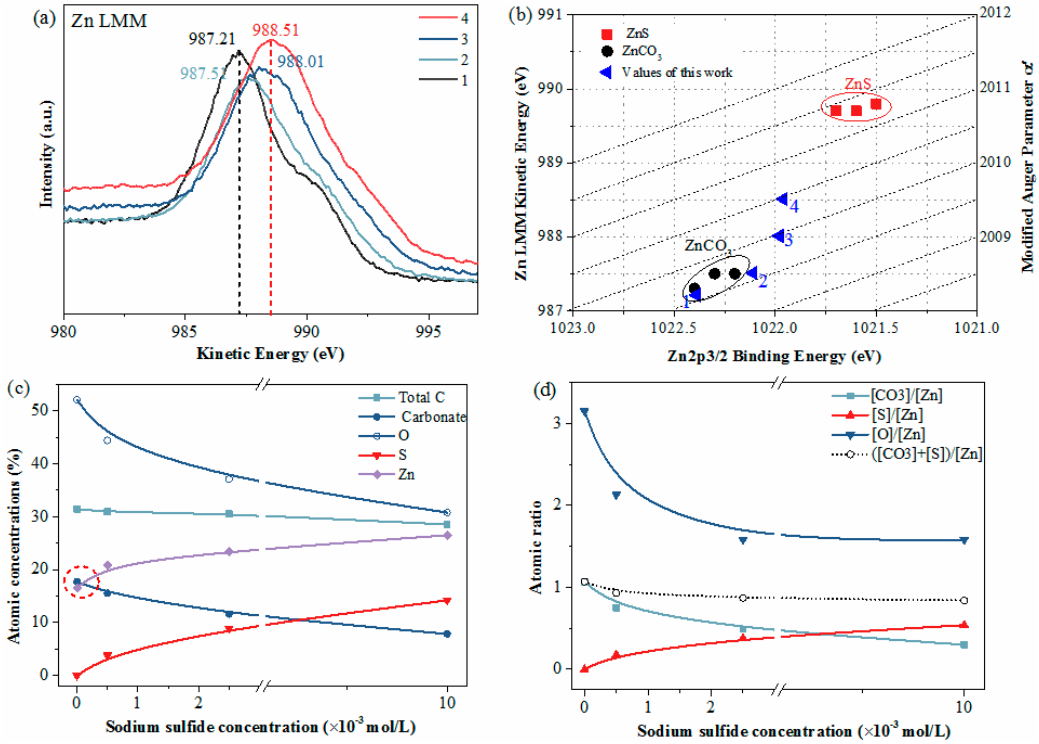

Figure 6. XPS Zn LMM spectra (**a**) and modified Auger parameter plot of Zn data (**b**) of smithsonite samples treated with (1) 0, (2) 0.5× 10^{-3}, (3) 2.5× 10^{-3} and (4) 10 × 10^{-3} mol/L $Na_2S{\cdot}9H_2O$. Atomic concentration (**c**) and atomic ration (**d**) of smithsonite as a function of Na_2S concentration; the concentrations of total C, O, Zn and S were calculated by C1s, O1s, Zn2p3 and S2p, respectively; the concentration of carbonate is the C concentration corresponding to C1s peak at around 290.00 eV.

3.3. AFM Observation

To observe the morphology changes of smithsonite before and after sulfidization, AFM height and phase imaging were used. In the AFM phase images, the presence of different materials at the surface of the sample was indicated by differences in contrast, providing additional information; hence, phase imaging is suitable for such a study [27,28].

As shown in Figure 7a, the unsulfidized smithsonite exhibited a relatively uniform surface morphology. However, some streaks generated during polishing were observed on the surfaces. After sulfidization, in contrast, some protrusions grew on the smithsonite at a high density (Figure 7(b1,b2)). Furthermore, significant differences in phase angle were observed.

AFM height profiles and phase shifts are respectively shown in Figure 8a,b. As depicted in Figure 8a, streaks on unsulfidized surfaces and protrusions on the sulfidized surfaces were reflected from the peaks and valleys of the height profile data, respectively. As plotted in Figure 8b, interestingly, no significant phase-angle differences were detected for the unsulfidized surfaces, further demonstrating its component homogeneity; however, large peaks and valleys emerged in the plot of the phase angle after sulfidization, further demonstrating the presence of more than one material.

AFM height imaging showed that sulfidization could significantly change the surface morphology of smithsonite. AFM phase imaging also demonstrated that sulfidization was localized on the smithsonite surface.

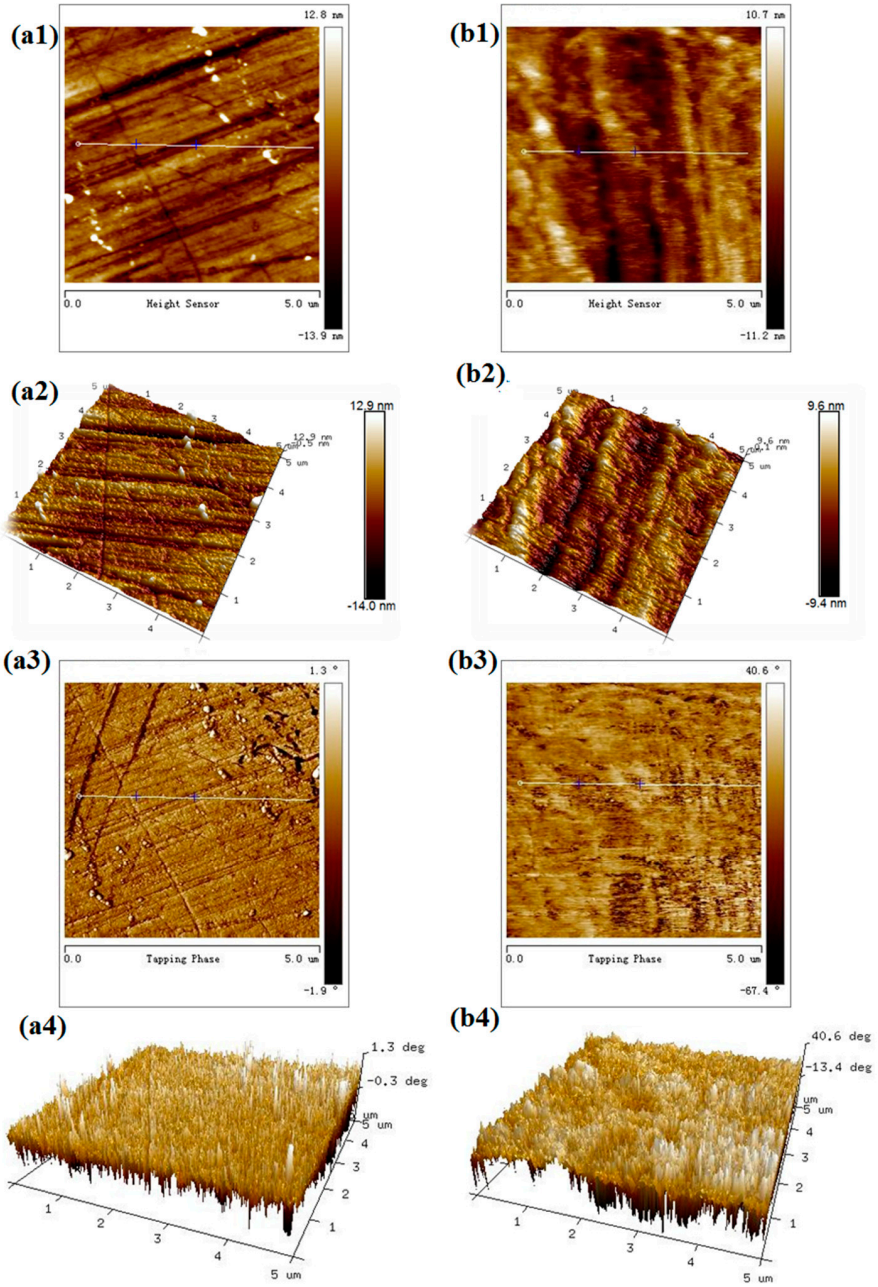

Figure 7. AFM 2D height (**a1**,**b1**), 3D height (**a2**,**b2**), 2D phase (**a3**,**b3**) and 3D phase (**a4**,**b4**) images of smithsonite treated with (**left**) 0 and (**right**) 10^{-2} mol /L Na_2S solution.

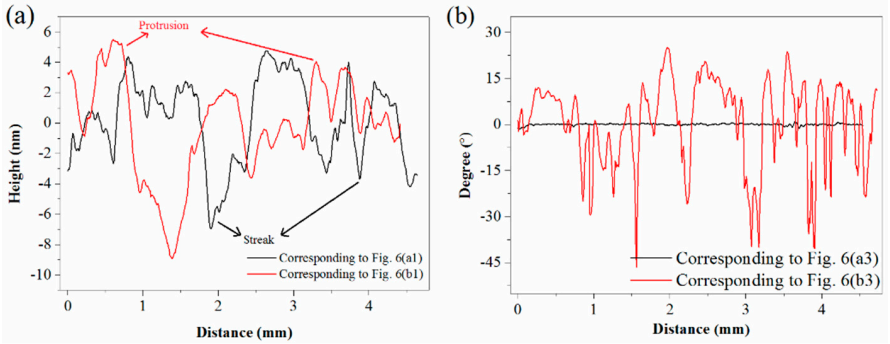

Figure 8. (**a**) Height profiles. (**b**) Phase shifts.

3.4. UV–Vis DRS Analysis

UV–vis DRS spectroscopy can be used to determine compositions [29,30]. As far as we know, this work represents the first report of the characterization of the composition of a sulfidized oxide mineral of a base metal using DRS spectra. Figure 9 shows the UV–vis DRS spectra of different samples. The spectra of both the unsulfidized smithsonite and the synthesized sphalerite ZnS showed absorption primarily in the UV region; however, the spectrum of the synthesized sphalerite ZnS exhibited a much broader absorption band, indicating substantially greater light absorbance. Two absorption peaks at ~214 and ~245 nm in the spectrum of the unsulfidized smithsonite and one absorption peak at ~303 nm in the spectrum of the synthesized ZnS were clearly observed. Interestingly, absorption peaks at ~303 nm emerged in the UV–vis DRS spectra of sulfidized samples, indicating the formation of ZnS. Notably, with increasing Na_2S concentration, the light absorbance of the sulfidized samples increased, especially in the UV light region, and peaks at ~214 and ~245 nm were gradually weakened, whereas the peak at ~303 nm gradually intensified, indicating that the ZnS content increased and the $ZnCO_3$ content decreased with increasing Na_2S concentration.

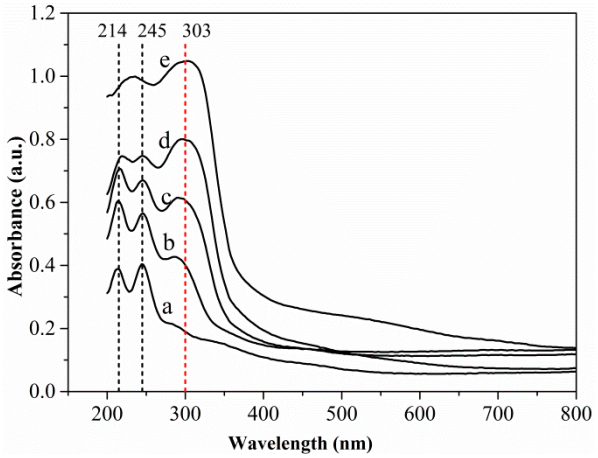

Figure 9. UV–vis DRS spectra of smithsonite treated with (**a**) 0, (**b**) 0.5×10^{-3}, (**c**) 2.5×10^{-3} and (**d**) 10×10^{-3} mol/L $Na_2S{\cdot}9H_2O$ and (**e**) synthesized sphalerite ZnS.

The UV–vis DRS spectra results further demonstrated the transformation of $ZnCO_3$ to ZnS during smithsonite sulfidization. Moreover, $ZnCO_3$ and ZnS were observed to coexist on the sulfidized smithsonite surfaces. Therefore, the UV–vis DRS results were consistent with the XPS results. The present work also shows that DRS can be used as a simple, inexpensive and sensitive methodology to characterize the composition at the surfaces of minerals.

3.5. Sulfidization Mechanism

ZnS has two basic structures, namely the sphalerite structure and the wurtzite structure. Accordingly, smithsonite sulfidization can occur under weak alkaline conditions according to the following reactions:

$$ZnCO_3(s) + HS^-(aq) = ZnS(\text{sphalerite}) + HCO_3{}^-(aq) \quad (2)$$

$$ZnCO_3(s) + HS^-(aq) = ZnS(\text{wurtzite}) + HCO_3{}^-(aq) \quad (3)$$

Equation (2) shows the sulfidization reaction leading to the formation of sphalerite-structured ZnS, and Equation (3) presents the sulfidization reaction leading to wurtzite-structured ZnS. As plotted in Figure 10a, the free energies of the two reactions were negative in the temperature range 273.15–303.15 K. Thus, the formation of both sphalerite ZnS and wurtzite ZnS was thermodynamically favorable. Figure 10b–d show unit-cell models of smithsonite $ZnCO_3$, sphalerite-structured ZnS

and wurtzite-structured ZnS, respectively, where the microstructural variations between the two sulfidization reactions are highlighted. Under ambient conditions, sphalerite-structured ZnS is the most stable phase, whereas wurtzite-structured ZnS is a thermodynamically metastable phase [31,32]. In addition, our UV–vis DRS spectra of the sulfidized smithsonite samples showed the characteristic absorption of sphalerite-structured ZnS but none of the characteristics observed in the UV–vis spectra of wurtzite-structured ZnS reported elsewhere [32]. Hence, sphalerite-structured ZnS is more likely to be the sulfidization product of smithsonite under flotation-relevant conditions.

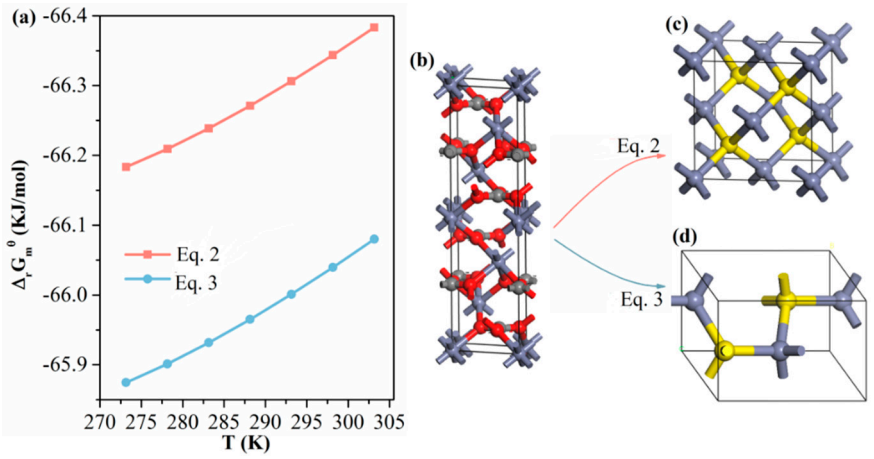

Figure 10. (**a**) $\Delta_r G_m^{\theta}$ vs. temperature plot of Equations (2) and (3) calculated using HSC Chemistry ver.6.0 (Outokumpu Research, Pori, Finland); the relevant thermodynamic data are presented in Tables S1 and S2. Unit cell models of (**b**) smithsonite $ZnCO_3$, (**c**) sphalerite-structured ZnS and (**d**) wurtzite-structured ZnS.

On the basis of the aforementioned characterizations and analyses, we proposed a model of a sulfidized smithsonite particle that shows the sulfidization product (sphalerite ZnS) grown on smithsonite (Figure 11). It can be concluded that smithsonite sulfidization is clearly a heterogeneous solid–liquid reaction in which the solid product adheres to the surfaces of unreacted smithsonite. Admittedly, such a reaction involves diffusion, adsorption and reaction. With diffusion and adsorption, the sulfide species react with $ZnCO_3$ at the smithsonite particles' surfaces, resulting in ZnS that nucleates and grows at the smithsonite–aqueous interface. Therefore, smithsonite sulfidization involves heterogeneous nucleation and growth of ZnS nuclei. All of our results are consistent with the coexistence of $ZnCO_3$ and ZnS on the sulfidized smithsonite surfaces, suggesting the formation of ZnS island structures, as illustrated in Figure 11. This behavior might be attributable to ZnS nuclei forming preferentially in the regions with high reactivity. It should also be noted that the degree of sulfidization increased with increasing Na_2S concentration, which was proven by the XPS and UV–vis DRS spectra results. However, this increase is not linear; when the concentration of sodium sulfide reached a certain value, the newly formed ZnS could hinder the sulfidization of unreacted smithsonite due to diffusion control.

As Lai et al. [10] demonstrated using ToF-SIMS and principal component analysis, sulfidization renders DDA amenable to interactions with the smithsonite surface. In fact, the interaction of the sulfidized smithsonite with DDA comes directly from the interaction of the surfaces of the newly formed ZnS phase with DDA. Therefore, further work is required to probe the surface differences between $ZnCO_3$ and ZnS in the interaction with water and DDA at the molecular level, which is responsible for the hydrophobicity and reactivity with DDA of smithsonite before and after sulfidization. In this communication, atomistic simulations can provide deeper understanding [33–40]. On the other hand, the AFM images showed that the particle surfaces became rougher; whether this change affects the rate of bubble–particle interaction and then flotation also needs further study.

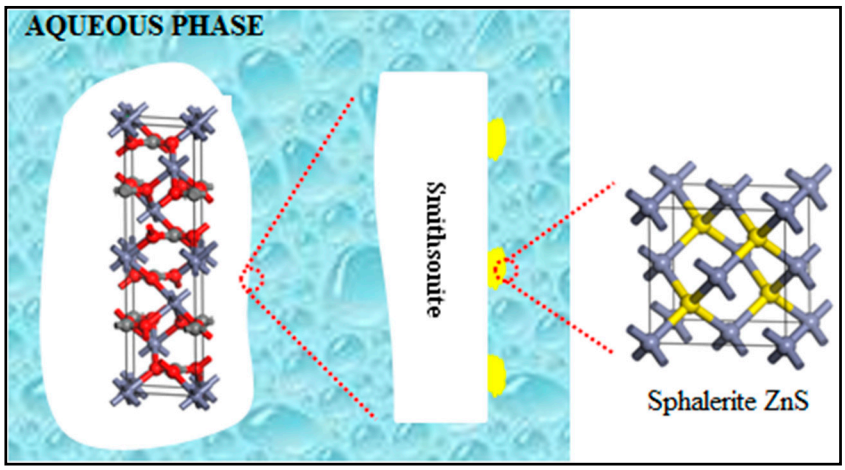

Figure 11. A model of the sulfidized smithsonite particle that shows ZnS island structures (in yellow) grown on smithsonite (in white).

4. Conclusions

This work provides strong evidence that smithsonite sulfidization is a transformation of $ZnCO_3$ to ZnS on smithsonite surfaces. However, this transformation is localized, resulting in the coexistence of $ZnCO_3$ and ZnS on sulfidized smithsonite surfaces or in the formation of ZnS island structures. Smithsonite sulfidization is clearly a heterogeneous solid–liquid reaction in which the solid product adheres at the surfaces of unreacted smithsonite. Smithsonite sulfidization involves heterogeneous nucleation and growth of ZnS nuclei. The ZnS might nucleate and grow preferentially in the regions with high reactivity, resulting in the localization of sulfidization. In addition, sphalerite-structured ZnS is more likely to be the sulfidization product of smithsonite under flotation-relevant conditions.

Supplementary Materials: The following are available online at http://www.mdpi.com/2075-163X/10/4/370/s1, Table S1: Thermodynamic data for Equation (2); Table S2: Thermodynamic data for Equation (3).

Author Contributions: Conceptualization, R.L. and J.L.; Data curation, J.L.; Formal analysis, R.L.; Funding acquisition, D.L.; Investigation, R.L. and J.L.; Methodology, R.L.; Project administration, D.L.; Resources, B.P., Z.L. and Y.W.; Software, B.P. and J.L.; Supervision, D.L.; Validation, Z.L.; Writing—original draft, R.L. All authors have read and agreed to the published version of the manuscript.

Funding: This research was funded by the National Natural Science Foundation of China, Grant No. 51264019.

Acknowledgments: We thank the Shiyanjia lab (www.shiyanjia.com) for the AFM and XPS measurements.

Conflicts of Interest: The authors declare no conflict of interest.

References

1. Boni, M.; Mondillo, N. The "Calamines" and the "Others": The great family of supergene nonsulfide zinc ores. *Ore Geol. Rev.* **2015**, *67*, 208–233. [CrossRef]
2. Feng, Q.C.; Wen, S.M. Formation of zinc sulfide species on smithsonite surfaces and itsresponse to flotation performance. *J. Alloys Compd.* **2017**, *709*, 602–608. [CrossRef]
3. Liu, C.; Zhang, W.; Song, S.; Li, H.; Liu, Y. Flotation separation of smithsonite from calcite using 2-phosphonobutane-1,2,4-tricarboxylic acid as a depressant. *Powder Technol.* **2019**, *352*, 11–15. [CrossRef]
4. Liu, C.; Zhu, G.; Song, S.; Li, H. Flotation separation of smithsonite from quartz using calcium lignosulphonate as a depressant and sodium oleate as a collector. *Miner. Eng.* **2019**, *131*, 385–391. [CrossRef]
5. Ejtemaei, M.; Gharabaghi, M.; Irannajad, M. A review of zinc oxide mineral beneficiation using flotation method. *Adv. Colloid Interface Sci.* **2014**, *206*, 68–78. [CrossRef]
6. Fa, K.Q.; Miller, J.D.; Jiang, T.; Li, G.H. Sulphidization flotation for recovery of lead and zinc from oxide-sulfide ores. *Trans. Nonferr. Met. Soc. China* **2005**, *15*, 1138–1144.
7. Luo, B.; Liu, Q.; Deng, J.; Li, S.; Yu, L.; Lai, H. Determining the lead-sulfur species formed on smithsonite surfaces during lead-ion enhanced sulfidation processing. *Appl. Surf. Sci.* **2020**, *506*, 144628. [CrossRef]

8. Jia, K.; Feng, Q.; Zhang, G.; Ji, W.; Zhang, G.-F.; Yang, B. The role of S(II) and Pb(II) in xanthate flotation of smithsonite: Surface properties and mechanism. *Appl. Surf. Sci.* **2018**, *442*, 92–100. [CrossRef]
9. Deng, R.; Hu, Y.; Ku, J.; Zuo, W.; Yang, Z. Adsorption of Fe(III) on smithsonite surfaces and implications for flotation. *Colloids Surf. A Physicochem. Eng. Asp.* **2017**, *533*, 308–315. [CrossRef]
10. Lai, H.; Deng, J.; Wen, S. Application of ToF-SIMS and PCA to study interaction mechanism of dodecylamine and smithsonite. *Appl. Surf. Sci.* **2019**, *496*, 143698. [CrossRef]
11. Luo, B.; Liu, Q.; Deng, J.; Yu, L.; Lai, H.; Song, C.; Li, S. Characterization of sulfide film on smithsonite surface during sulfidation processing and its response to flotation performance. *Powder Technol.* **2019**, *351*, 144–152. [CrossRef]
12. Garbassi, F.; Marabini, A.M. Spectroscopic investigation of sulphidation of zinc and lead carbonates. *J. Chem. Soc. Faraday Trans. 1 Phys. Chem. Condens. Phases* **1986**, *82*, 2043. [CrossRef]
13. Wu, D.; Wen, S.; Deng, J.; Liu, J.; Mao, Y. Study on the sulfidation behavior of smithsonite. *Appl. Surf. Sci.* **2015**, *329*, 315–320. [CrossRef]
14. Zhao, W.; Liu, D.; Feng, Q.; Wen, S.; Chang, W. DFT insights into the electronic properties and adsorption mechanism of HS− on smithsonite (1 0 1) surface. *Miner. Eng.* **2019**, *141*, 105846. [CrossRef]
15. Chen, Y.; Liu, M.; Chen, J.; Li, Y.; Zhao, C.; Mu, X. A density functional based tight binding (DFTB+) study on the sulfidization-amine flotation mechanism of smithsonite. *Appl. Surf. Sci.* **2018**, *458*, 454–463. [CrossRef]
16. Liu, J.; Zeng, Y.; Ejtemaei, M.; Nguyen, A.V.; Wang, Y.; Wen, S. DFT simulation of S-species interaction with smithsonite (0 0 1) surface: Effect of water molecule adsorption position. *Results Phys.* **2019**, *15*, 102575. [CrossRef]
17. Liu, R.Z.; Liu, D.W.; Li, J.L.; Liu, S.Y.; Liu, Z.C.; Gao, L.Q.; Jia, X.D.; Ao, S.F. Improved understanding of the sulfidization mechanism in cerussite flotation: An XPS, ToF-SIMS and FESEM investigation. *Colloid. Surf. A* **2020**, *595*, 124508. [CrossRef]
18. Zhao, Y.; Kang, S.; Qin, L.; Wang, W.; Zhang, T.; Song, S.; Komarneni, S. Self-assembled gels of Fe-chitosan/montmorillonite nanosheets: Dye degradation by the synergistic effect of adsorption and photo-Fenton reaction. *Chem. Eng. J.* **2020**, *379*, 122322. [CrossRef]
19. Frateur, I.; Lecoeur, J.; Zanna, S.; Olsson, C.; Landolt, D.; Marcus, P. Adsorption of BSA on passivated chromium studied by a flow-cell EQCM and XPS. *Electrochim. Acta* **2007**, *52*, 7660–7669. [CrossRef]
20. Peng, W.; Han, G.; Cao, Y.; Sun, K.; Song, S. Efficiently removing Pb(II) from wastewater by graphene oxide using foam flotation. *Colloids Surf. A Physicochem. Eng. Asp.* **2018**, *556*, 266–272. [CrossRef]
21. Available online: https://xpssimplified.com/elements/zinc.php (accessed on 29 March 2020).
22. Buckley, A.; Wouterlood, H.; Woods, R. The surface composition of natural sphalerites under oxidative leaching conditions. *Hydrometallurgy* **1989**, *22*, 39–56. [CrossRef]
23. Deroubaix, G.; Marcus, P. X-ray photoelectron spectroscopy analysis of copper and zinc oxides and sulphides. *Surf. Interface Anal.* **1992**, *18*, 39–46. [CrossRef]
24. Laajalehto, K.; Kartio, I.; Nowak, P. XPS study of clean metal sulfide surfaces. *Appl. Surf. Sci.* **1994**, *81*, 11–15. [CrossRef]
25. Lai, H.; Deng, J.; Wen, S.; Liu, Q. Elucidation of lead ions adsorption mechanism on marmatite surface by PCA-assisted ToF-SIMS, XPS and zeta potential. *Miner. Eng.* **2019**, *144*, 106035. [CrossRef]
26. Dake, L.S.; Baer, D.R.; Zachara, J.M. Auger parameter measurements of zinc compounds relevant to zinc transport in the environment. *Surf. Interface Anal.* **1989**, *14*, 71–75. [CrossRef]
27. Jovanov, V.; Yumnam, N.; Müller, A.; Gruber, M.; Wagner, V. Determining Material-Specific Morphology of Bulk-Heterojunction Organic Solar Cells Using AFM Phase Imaging. *J. Phys. Chem. C* **2017**, *121*, 9173–9180. [CrossRef]
28. O'Nei, K.D.; Semenikhin, O.A.; O'Neil, K. AFM Phase Imaging of Electropolymerized Polybithiophene Films at Different Stages of Their Growth. *J. Phys. Chem. C* **2007**, *111*, 14823–14832. [CrossRef]
29. Rossel, R.A.V.; McGlynn, R.; McBratney, A.B. Determining the composition of mineral-organic mixes using UV–vis–NIR diffuse reflectance spectroscopy. *Geoderma* **2006**, *137*, 70–82. [CrossRef]
30. Zanjanchi, M.A.; Noei, H.; Moghimi, M. Rapid determination of aluminum by UV–vis diffuse reflectance spectroscopy with application of suitable adsorbents. *Talanta* **2006**, *70*, 933–939. [CrossRef]
31. Banerjee, I.A.; Yu, L.; Matsui, H. Room-Temperature Wurtzite ZnS Nanocrystal Growth on Zn Finger-like Peptide Nanotubes by Controlling Their Unfolding Peptide Structures. *J. Am. Chem. Soc.* **2005**, *127*, 16002–16003. [CrossRef]

32. Liang, X.; Xing, L.; Xiang, J.; Zhang, F.; Jiao, J.; Cui, L.; Song, B.; Chen, S.; Zhao, C.; Sai, H. The Role of the Liquid–Liquid Interface in the Synthesis of Nonequilibrium Crystalline Wurtzite ZnS at Room Temperature. *Cryst. Growth Des.* **2012**, *12*, 1173–1179. [CrossRef]
33. Badawi, M.; Cristol, S.; Paul, J.-F.; Payen, E. DFT study of furan adsorption over stable molybdenum sulfide catalyst under HDO conditions. *ComptesRendusChim.* **2009**, *12*, 754–761. [CrossRef]
34. Badawi, M.; Paul, J.; Cristol, S.; Payen, E.; Romero, Y.; Richard, F.; Brunet, S.; Lambert, D.; Portier, X.; Popov, A.; et al. Effect of water on the stability of Mo and CoMo hydrodeoxygenation catalysts: A combined experimental and DFT study. *J. Catal.* **2011**, *282*, 155–164. [CrossRef]
35. Foucaud, Y.; Badawi, M.; Filippov, L.O.; Filippova, I.V.; Lébegue, S. Surface Properties of Fluorite in Presence of Water: An Atomistic Investigation. *J. Phys. Chem. B* **2018**, *122*, 6829–6836. [CrossRef]
36. Bandura, A.V.; Kubicki, J.D.; Sofo, J. Periodic Density Functional Theory Study of Water Adsorption on the α-Quartz (101) Surface. *J. Phys. Chem. C* **2011**, *115*, 5756–5766. [CrossRef]
37. Souvi, S.M.O.; Badawi, M.; Virot, F.; Cristol, S.; Cantrel, L.; Paul, J.-F. Influence of water, dihydrogen and dioxygen on the stability of the Cr_2O_3 surface: A first-principles investigation. *Surf. Sci.* **2017**, *666*, 44–52. [CrossRef]
38. Foucaud, Y.; Badawi, M.; Filippov, L.; Filippova, I.; Lébegue, S. A review of atomistic simulation methods for surface physical-chemistry phenomena applied to froth flotation. *Miner. Eng.* **2019**, *143*, 106020. [CrossRef]
39. Foucaud, Y.; Lebègue, S.; Filippov, L.O.; Filippova, I.V.; Badawi, M. Molecular Insight into Fatty Acid Adsorption on Bare and Hydrated (111) Fluorite Surface. *J. Phys. Chem. B* **2018**, *122*, 12403–12410. [CrossRef]
40. Foucaud, Y.; Badawi, M.; Filippov, L.O.; Barres, O.; Filippova, I.V.; Lébegue, S. Synergistic adsorptions of Na_2CO_3 and Na_2SiO_3 on calcium minerals revealed by spectroscopic and ab initio molecular dynamics studies. *Chem. Sci.* **2019**, *10*, 9928–9940. [CrossRef]